scientific reports

OPEN

Efficient calculation and analysis of dynamic RCS characteristics for moving target using the shooting and bouncing rays method

Wenxing Wu, Jinzu Ji, Ke Chen, Guoxu Chen, Shunli Sun, Zhikai Guo & Yunpeng Ma

The rapid solution of RCS for moving targets is of great significance for the detection and identification of targets. This paper proposes an efficient shooting and bouncing rays (SBR) method for calculating the electromagnetic (EM) scattering of moving targets. The main idea is to reduce the number of tracked rays and avoid the splitting of the ray tubes by using dense rays instead of the ray tubes. The efficient ray-tracing kernel Embree is used to accelerate the intersection detection of rays and target geometry through the boundary volume hierarchy (BVH) tree. In addition, the CPU parallel acceleration technology is used to accelerate the solution of the RCS scattering field. The entire solution process is carried out on the CPU, avoiding the disadvantages of OptiX's high dependence on NVIDIA's GPU hardware and the complexity of CPU-GPU data transmission. Finally, time-frequency analysis technology is used in the analysis of scattering characteristics for moving targets. Meanwhile, combined with the high-resolution range profile (HRRP), it can reveal the frequency modulation characteristics in the target motion, providing important information for identification, classification, and motion parameter estimation of the targets.

Radar cross section (RCS) is a critical parameter to quantify the reflection ability of a target to radar signal. The precise acquisition of RCS serves as the foundation for accurate detection and recognition[1,2]. In recent years, with the continuous development of computational electromagnetic (EM), the methods for solving EM scattering have become increasingly comprehensive and mature. Among them, the low-frequency accurate calculation methods of RCS mainly include the method of moments (MoM)[3] and the multilevel fast multipole method (MLFMM)[4] based on integral equation solving, the finite difference time domain (FDTD)[5] for simulating the propagation process of EM wave, and the finite element method (FEM)[6] based in variational principle and functional analysis. However, although the above methods have high accuracy, they are limited by computational resources and time when applied to electrically large targets. Therefore, high-frequency approximation algorithms with high computational efficiency and broad applicability are predominantly employed for such targets[7]. These methods include physical optics (PO)[8], geometrical optics (GO)[9], physical theory of diffraction (PTD)[10], and the method of equivalent currents (MEC)[11]. As a hybrid method combining GO and PO, the shooting and bouncing ray (SBR) utilizes the ray-tracing principle of GO and the induced current calculation principle of PO. The SBR overcomes the defect that GO fails in the caustic region and PO cannot calculate the multiple scattering effect[12].

At present, the SBR method primarily focuses on improving computational accuracy and efficiency. On the basis of ray-tracing, combining the uniform theory of diffraction (UTD) and PTD can make up for the deficiency of SBR and solve the problem of no electric field and boundary discontinuity in shadow region[13,14]. In addition, Cong et al. proposed a correction to the target scattering field by incorporating non-specular scattering mechanisms obtained in the sidelobe direction into the radiation effect[13]. In terms of improving computational efficiency, the primary strategies are reducing the number of ray tubes and accelerating ray-tracing. In addition to the algorithm based on traditional octree or Kd-tree to divide the structure space to speed up ray-tracing, the Guo Lixin team adopted the neighborhood search technique to speed up the ray-tracing process[15,16] and proposed a rope-based Kd-tree data structure with good performance[17]. In addition, the boundary volume hierarchy (BVH) tree is also a good structure for accelerating ray intersection detection[18]. Wei et al. used a scanline algorithm to convert three-dimensional processing into a two-dimensional graphical representation, thereby accelerating shadow elimination[19]. To address the issue of increasing the number of rays with frequency and the splitting of ray tubes in forward tracing algorithms, the application of backward tracing

School of Aeronautic Science and Engineering, Beihang University, Beijing 100191, China. email: ma_yun_peng@126.com

techniques reduces intersection tests between rays and unnecessary facets[14,17,20]. By combining the advantages of forward and backward tracing, bidirectional ray-tracing was established to accelerate the ray-tracing process and compute more scattering mechanisms[13]. To reduce the number of rays to be traced, the improved SBR using ray refinement reduces the number of rays and tracing times[21]. Huo et al. utilized rays instead of ray tubes and constructed a virtual ray tube at the ray exit for PO integration, effectively decreasing the number of rays requiring tracking[22]. Furthermore, with the continuous development of graphics processing unit (GPU) technology, an increasing number of researchers are leveraging GPU parallel acceleration techniques based on the CUDA framework and the open graphics library (OpenGL) framework to enhance the efficiency of ray-tracing[12,15,16]. The real-time ray-tracing based on OPTIX is also used to accelerate the SBR method[23].

The rapid solution and analysis of RCS scattering characteristics based on moving targets is of great significance in practical detection environments. Huang et al. developed a dynamic volume equivalent SBR method for solving the scattering of moving targets on the sea surface[1]. Meng and Xi introduced an improved hybrid-tree based SBR method for complex moving multi-targets[24,25]. Researchers have conducted studies on dynamic RCS simulation methods for the multi-modal flight of tilt-rotor aircraft[26,27] and the dynamic flight motion of unmanned aerial vehicles[28,29]. However, most studies have low efficiency in calculating dynamic RCS for moving targets. Although the computing efficiency based on GPU architecture is relatively high, it still faces the disadvantages of complex data transmission between CPU-GPU and high dependence on NVIDIA's GPU hardware. The development of the kernel framework Embree for efficient CPU ray-tracing has achieved performance comparable to that of OPTIX[30]. Therefore, to meet the huge amount of calculations for solving the dynamic RCS of moving targets, we hope to propose a more efficient SBR method based only on CPU architecture while ensuring accuracy.

In this paper, we first established a detection model for moving targets to calculate the radar detection angle in real time. Subsequently, we proposed a method that utilizes dense rays to replace ray tubes, thereby reducing the number of traced rays and circumventing the challenges associated with ray tube splitting. Additionally, the Embree kernel framework was utilized to fully harness the CPU's performance to achieve high-performance ray-tracing. Among them, the BVH tree was used to accelerate the intersection detection between rays and target geometry. Furthermore, we introduced the PTD method to compensate for the computational loss caused by edge diffraction and improve the calculation accuracy. Finally, our method was compared with the computational cost of MLFMM and RL-GO in FEKO, and time-frequency analysis techniques were also used to analyze the micro-Doppler characteristics during the micro-motion process of moving targets.

Efficient SBR solution for EM scattering of moving targets

Moving target modeling

Target motion modeling is a premise for solving and analyzing the EM scattering of moving targets. Although the radial motion of the target relative to the radar induces changes in the phase of the radar echo signal, the motion speed of target changes slowly compared to the propagation speed of EM wave. And the resulting Doppler frequency is well below the basic frequency of the EM wave. Therefore, a dynamic process can be approximated as a sequence of stationary states in sufficiently short time intervals. This sequence permits the application of frequency-domain EM simulation techniques to efficiently solve the time domain information of target. Based on this core assumption, the quasi-static method is applied to EM scattering modeling of moving targets.

In three-dimensional space, translation and rotation are two fundamental operations used to describe the relative motion of a target or coordinate system. The homogeneous transformation integrates translation and rotation into a 4×4 matrix T through homogeneous coordinates, achieving unified representation and efficient computation:

$$\mathrm{T}=\begin{bmatrix}\mathrm{R} & \mathrm{t}\\ 0 & 1\end{bmatrix}=\begin{bmatrix}\cos\theta+u_x^2(1-\cos\theta) & u_xu_y(1-\cos\theta)-u_z\sin\theta & u_xu_z(1-\cos\theta)+u_y\sin\theta & t_x\\ u_yu_x(1-\cos\theta)+u_z\sin\theta & \cos\theta+u_y^2(1-\cos\theta) & u_yu_z(1-\cos\theta)-u_x\sin\theta & t_y\\ u_zu_x(1-\cos\theta)-u_y\sin\theta & u_zu_y(1-\cos\theta)+u_x\sin\theta & \cos\theta+u_z^2(1-\cos\theta) & t_z\\ 0 & 0 & 0 & 1\end{bmatrix} \tag{1}$$

where, the rotation matrix R (3×3) describes the axial variation of the coordinate system, and the translation vector $\mathrm{t}=[t_x,t_y,t_z]^{\mathrm{T}}$ (3×1) describes the displacement of the origin of the coordinate system. The scalar 1 ensures consistency in homogeneous coordinate operations. The target rotates around the rotation axis $\mathrm{u}=[u_x,u_y,u_z]^{\mathrm{T}}$ by an angle θ at a certain moment. It is assumed that the target's coordinate in the radar coordinate system is $[x_t,y_t,z_t]^{\mathrm{T}}$. According to the coordinate transformation rule between coordinate systems, the radar's coordinate $[x_r,y_r,z_r]^{\mathrm{T}}$ in the target coordinate system can be expressed as:

$$[x_r,y_r,z_r,1]^{\mathrm{T}}=\mathrm{T}\cdot[0-x_t,0-y_t,0-z_t,1]^{\mathrm{T}} \tag{2}$$

The target coordinate system defined in this article is shown in Fig. 1. The *x*-axis points to the head direction, the *y*-axis points to the left along the target axis, and the *z*-axis is oriented perpendicularly upward from the xoy plane, adhering to the right-handed coordinate system convention. The radar elevation angle θ_r is defined as the angle between the origin-radar line and the positive *z*-axis direction, and the radar azimuth angle φ_r is defined as the angle between the projection of the origin-radar line in the *xoy* plane and the positive *x*-axis. According to the geometric relationship, the elevation and azimuth angle of the radar in the target system can be calculated by:

$$\varphi_r=\begin{cases}\arccos\frac{x_r}{\sqrt{{x_r}^2+{y_r}^2}}, y_r\geq 0\\ \arccos\frac{-x_r}{\sqrt{{x_r}^2+{y_r}^2}}, y_r<0\end{cases} \tag{3}$$

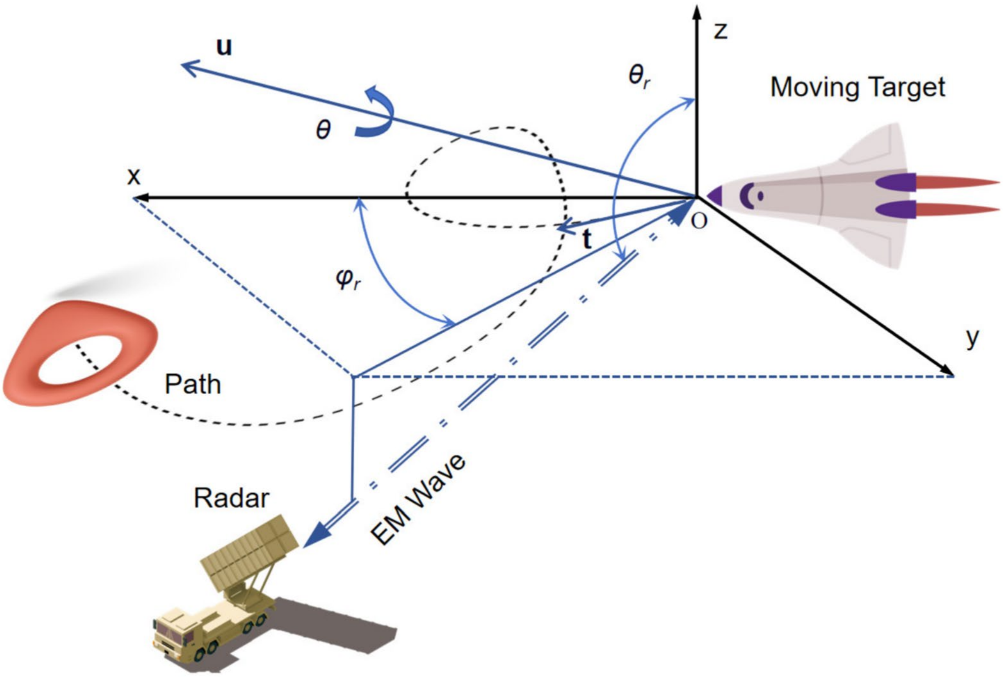

Fig. 1. The radar detection modeling of moving targets.

$$\theta_r = \arccos \frac{z_r}{\sqrt{{x_r}^2 + {y_r}^2 + {z_r}^2}} \tag{4}$$

Based on the relative position between the target and the radar, as well as the target's translational and rotational states, the elevation angle and azimuth angle are calculated. These angles are then utilized to solve for the dynamic RCS of the moving target at each moment.

Efficient SBR method

Dense rays instead of ray tubes

When EM wave illuminates the target surface, the scattering field is excited by the interaction between the scatterer and the EM wave. The SBR theory combines the theory of GO and PO to calculate the scattering field by tracing the propagation path of rays on the target surface. The basic principle of this method is to first unfold uniformly incident plane waves into a dense set of parallel ray tubes, and assume that the propagation of EM wave follows the laws of GO. By simulating the characteristics of EM wave in the process of multiple reflection and diffraction on the surface of the target, the RCS of the target can be effectively predicted.

To accurately simulate the propagation and scattering of EM wave on the surfaces of complex targets, it is usually necessary to generate a large number of ray tubes. In the process of propagation, these ray tubes will be intersected and updated with the target surface many times, resulting in a large amount of computation and low computation efficiency. In addition, the problem of ray tube splitting occurs when the ray tube illuminates the edge of target, which will also affect the calculation accuracy and increase the complexity of tube tracing. It is considered that the scattering contribution of the first reflection of the EM wave is usually the largest in the integral calculation of SBR method. Therefore, we replace the traditional ray tube with a dense single ray, and replace the ray tube density with the encrypted discrete triangular facets. This measure reduces the number of tracked rays and memory loss and avoids the computational difficulties caused by the splitting of the ray tubes. We set the initial parallel rays to pass through the center of the first illuminated facets, and any facet that intersects with multiple reflected rays is considered an integrated facet.

Ray-tracing based on Embree

In the process of calculating the RCS of target using the SBR method, the intersection detection of rays and target geometry is the most time-consuming step. Embree is an efficient ray-tracing kernel framework developed by Intel. Because Embree is based on an efficient CPU architecture to achieve ray-tracing, it avoids the drawbacks of OptiX's high dependence on NVIDIA's GPU hardware and the complexity of CPU-GPU data transfer.

The BVH tree is used to accelerate the detection of the intersection between rays and target in Embree. As shown in Fig. 2, the BVH tree divides the scene into a series of hierarchical bounding boxes, each containing a portion of the geometry in the scene. In ray intersection detection, the first step is to check whether the ray intersects with the bounding box of the root node. If it does not intersect, there is no need to further check the leaf nodes of the current node, thus avoiding a lot of unnecessary intersection calculations. When dealing with simple and compact grid models, BVH tree partition using a uniform segmentation strategy usually gets

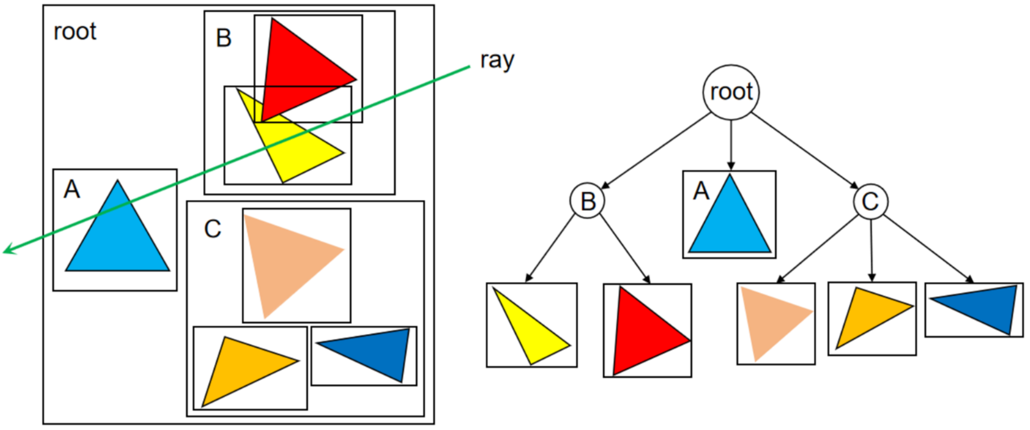

Fig. 2. The schematic diagram of BVH tree principle.

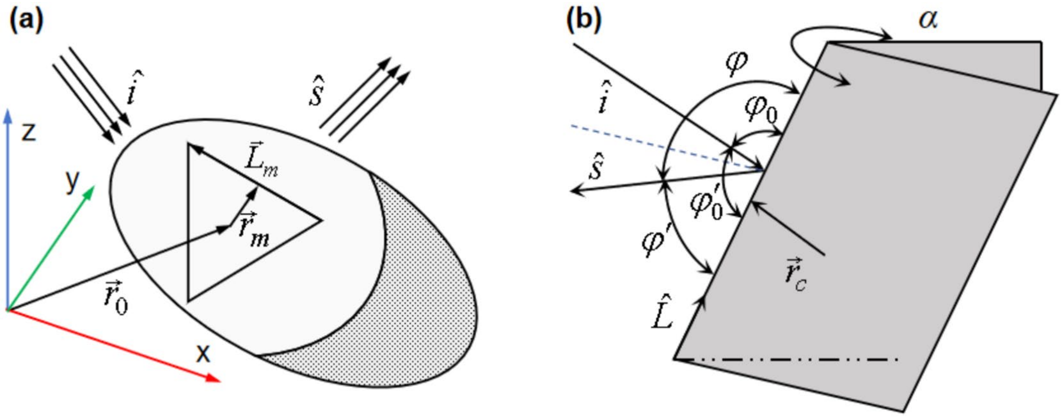

Fig. 3. The schematic diagram of EM scattering: **(a)** PO method. **(b)** PTD method.

good results. But when there is a large amount of overlap in the bounding boxes of the scene, the surface area heuristic (SAH) method is used to optimize the construction of BVH tree. Aim to dynamically select the optimal segmentation position based on the SAH cost function, to minimize the weighted cost of the surface area and geometric distribution of leaf nodes.

Scattering field solution

The scattering field of an electrically-large complex target includes a reflection field and a diffraction field. There are usually specular reflection, edge diffraction, and creeping wave diffraction. Under the condition of high-frequency approximation, the details regarding the generation and slow attenuation of creeping wave along the surface have relatively minor impacts on the overall distribution of the EM field. Consequently, only specular reflection and edge diffraction are considered in our research. Although surface creeping wave can significantly contribute to backward scattering at grazing angles, their impact on the overall scattering is often secondary to specular reflection and does not affect the analysis of the scattering characteristics of moving targets.

The PO method uses the induced current on the surface of the scatterer to replace the scatterer itself as the source of the scattering field, and then the surface induced current is integrated to solve the RCS of target. As shown in Fig. 3a, the PO method assumes that the induced current exists only in the region directly irradiated by the incident wave. Based on the principle of tangent plane approximation, the induced current can be expressed as:

$$\vec{J}_s = 2\hat{n} \times \vec{H}_i \tag{5}$$

where $\hat{n}$ is the outward unit normal vector of the surface, $\vec{H}_i$ is the intensity of the incident magnetic field. Based on the Stratton-Chu scattering integral equation, it can be deduced that the PO scattering contribution of a single triangular facet is:

$$\vec{E}_{PO} = \frac{e^{jk\vec{w}\cdot\vec{r}_m}}{\sqrt{\pi}|\vec{p}|^2}\hat{n}\cdot\left(\hat{e}_s \times \hat{h}_i\right)e^{jk\vec{w}\cdot\vec{r}_0}\sum_{m=1}^{3}\vec{p}\cdot\vec{L}_m \sin\text{c}\left(\frac{k\vec{w}\cdot\vec{L}_m}{2}\right) \tag{6}$$

where, *k* is the wave number of the incident wave, $\hat{e}_s$ and $\hat{h}_i$ represent the directions of the scattered electric field and the incident magnetic field, respectively. $\vec{w} = \hat{s} - \hat{i}$, where $\hat{s}$ and $\hat{i}$ are the unit vectors in the scattering direction and the incident direction, respectively. $\vec{r}_0$ represents the position vector of the source point, $|\vec{p}|$ represents the modulus length of $\hat{n} \times \hat{w}$, $\vec{r}_m$ is the position vector of the midpoint of the *m*-th edge relative to the source point, and $\vec{L}_m$ is the vector of the *m*-th edge of the facet.

Due to the lack of consideration for the influence of edge diffraction in the PO method, there is a significant loss in computational accuracy. Therefore, the PTD method can be introduced to correct the scattering field error caused by edge diffraction and improve the calculation accuracy. As shown in Fig. 3b, it is a wedge with the external wedge angle of α. Where $n = \alpha/\pi$ represents the normalized angle. The incidence and diffraction angle are φ_0 and φ, respectively. And $\varphi' = \alpha - \varphi$ and $\varphi'_0 = \alpha - \varphi_0$ are angles starting from another facet. In order to solve the singular value of GTD at the incident boundary and reflection boundary, the diffraction coefficients *f* and *g* of PTD are obtained by subtracting the singular term from the original GTD. Where $f = (X_1 + X_2) - (Y_1 + Y_2)$ and $g = (X_1 + X_2) + (Y_1 + Y_2)$. The other parameters are as follows:

$$\begin{array}{l}
X_1 = -\frac{1}{2n}\cot\frac{\pi-(\varphi-\varphi_0)}{2n} + \frac{U(\pi-\varphi_0)}{2}\cot\left(\frac{\pi-(\varphi-\varphi_0)}{2}\right)\\
X_2 = -\frac{1}{2n}\cot\frac{\pi-\left(\varphi'-\varphi'_0\right)}{2n} + \frac{U\left(\pi-\varphi'_0\right)}{2}\cot\left(\frac{\pi-\left(\varphi'-\varphi'_0\right)}{2}\right)\\
Y_1 = -\frac{1}{2n}\cot\frac{\pi-(\varphi+\varphi_0)}{2n} + \frac{U(\pi-\varphi_0)}{2}\cot\left(\frac{\pi-(\varphi+\varphi_0)}{2}\right)\\
Y_2 = -\frac{1}{2n}\cot\frac{\pi-\left(\varphi'+\varphi'_0\right)}{2n} + \frac{U\left(\pi-\varphi'_0\right)}{2}\cot\left(\frac{\pi-\left(\varphi'+\varphi'_0\right)}{2}\right)
\end{array} \tag{7}$$

where $U(x)$ is a step function, which is 1 when $x \geq 0$ and 0 when $x < 0$.

It is assumed that after the EM wave is irradiated to the edge, the diffraction field at a certain point is the sum of the diffraction effects from many points on the edge. Then the scattering field at the edge can be obtained by integrating the equivalent EM current of each diffraction point. When applying the concept of equivalent EM current, the diffracted field at the edge can be equivalently treated as the far-field of an infinitely long linear source. Therefore, the expressions for equivalent electric current density I_e and equivalent magnetic current density I_m represented by the diffraction coefficients of PTD:

$$\begin{array}{l}
I_e = \frac{2jk^2 f}{\omega\mu k_t^2}E_z^i\\
\\
I_m = \frac{2jk^2 g}{\omega\varepsilon k_t^2}H_z^i
\end{array} \tag{8}$$

where, E_z^i and H_z^i represent the z-component of the incident electric field and magnetic field, respectively. $k_t^2 = k^2 - k_z^2$, where k_z represents the component of wave number *k* in the z-direction. μ and ε represent the permittivity and permeability, respectively, while ω denotes the angular frequency. If the equivalent electric and magnetic current are regarded as finite-length linear sources located at the position of the finite-length edge, then the scattering field of the edge can be calculated as:

$$\vec{E}_{PTD} = \frac{\left|\vec{L}\right|}{\sqrt{\pi}\left(1 - \left|\hat{L}\cdot\hat{i}\right|^2\right)}\left[\left(\hat{L}\cdot\hat{e}_i\right)^2 f - \left(\hat{L}\cdot\hat{h}_i\right)^2 g\right]e^{jk\vec{w}\cdot\vec{r}_c}\sin\text{c}\frac{k\vec{w}\cdot\vec{L}}{2} \tag{9}$$

where $\vec{L}$ is the edge vector, $\left|\vec{L}\right|$ and $\hat{L}$ are the length and unit vector of the edge, respectively. $\hat{e}_i$ represents the direction of the incident electric field, and r_c is the position vector of the midpoint of the edge. Then the total scattering field of the target is:

$$\vec{E}_{total} = \vec{E}_{PO} + \vec{E}_{PTD} \tag{10}$$

CPU parallel acceleration

In order to further improve the efficiency of RCS calculation for moving targets, we adopt CPU parallel acceleration technology. In our study, we decompose the calculation process of RCS for moving targets into multiple independent subtasks, each corresponding to a specific time series. These subtasks are designed to be executed in parallel because there are no data dependencies between them. To achieve parallelization, we first define a function responsible for grid processing based on the different attitudes of the target at the current time step, and calculate the RCS of the target in the direction of radar incidence. Then, utilizing the parallel processing capability of multi-core CPUs, all computing tasks are automatically assigned to each process in the process pool, and the computation results of each process are collected.

The experimental results show that the efficiency of dynamic RCS calculation is significantly improved after adopting CPU parallel acceleration technology. Under the same computing resources, the total time consumption of parallel computing is reduced by at least 80% compared to serial computing. In particular, when there are more facets and a greater amount of computation, the acceleration effect is more obvious. This result indicates that CPU parallel acceleration technology has significant advantages in the large-scale RCS computation of moving target, and lays a foundation for the subsequent real-time radar signal time-frequency conversion.

Time-frequency analysis with micro-Doppler

Time-frequency analysis with micro-Doppler is a technique used in signal processing to analyze the scattering signal characteristics of moving targets such as rotating, vibrating, and complex moving targets. Combining the principle of time-frequency analysis and the micro-Doppler effect, it can reveal the subtle frequency modulation characteristics of target motion, and provide important information for target recognition, classification, and motion parameter estimation.

Short Time Fourier Transform (STFT) is a time-frequency analysis method used to analyze non-stationary signals. The basic idea is to divide a long-time non-stationary signal into multiple short-time stationary signals, and perform a Fourier transform on each short-time segment to obtain the joint distribution of the signal in both time domain and frequency domain. Due to the fact that the calculated dynamic RCS sequence is a discrete-time series, the sampling process converts the continuous-time signal $x\left(t\right)$ into a discrete-time signal $x\left[n\right]$ with a sampling frequency of f_s. The discrete form of STFT is represented as:

$$X\left(m,k\right)=\sum_{n=0}^{N-1}x\left[n\right]w\left[n-mR\right]e^{\frac{-j2\pi kn}{N}} \tag{11}$$

where, $w\left[n\right]$ is the discrete window function with length *N*. *R* is the frame shift, representing the step length of the window function movement. *m* and *k* are the indexes of the time frame and frequency, respectively.

For better understanding, Fig. 4 presents the flowchart of the efficient SBR method proposed in this paper for solving the dynamic RCS and micro-Doppler time-frequency analysis of moving target.

Results and discussion

In this section, we simulated the EM scattering of multiple targets using the efficient SBR method proposed in the previous section, and the geometric models used are shown in Fig. 5. And the accuracy and efficiency of the calculations were compared with the open-source program RaytrAMP (https://github.com/RedBlight/RaytrAMP) using the SBR method and MLFMM and RL-GO in the general EM simulation software FEKO2025. Then, the micro-Doppler frequency modulation characteristics of the moving targets were analyzed, including the

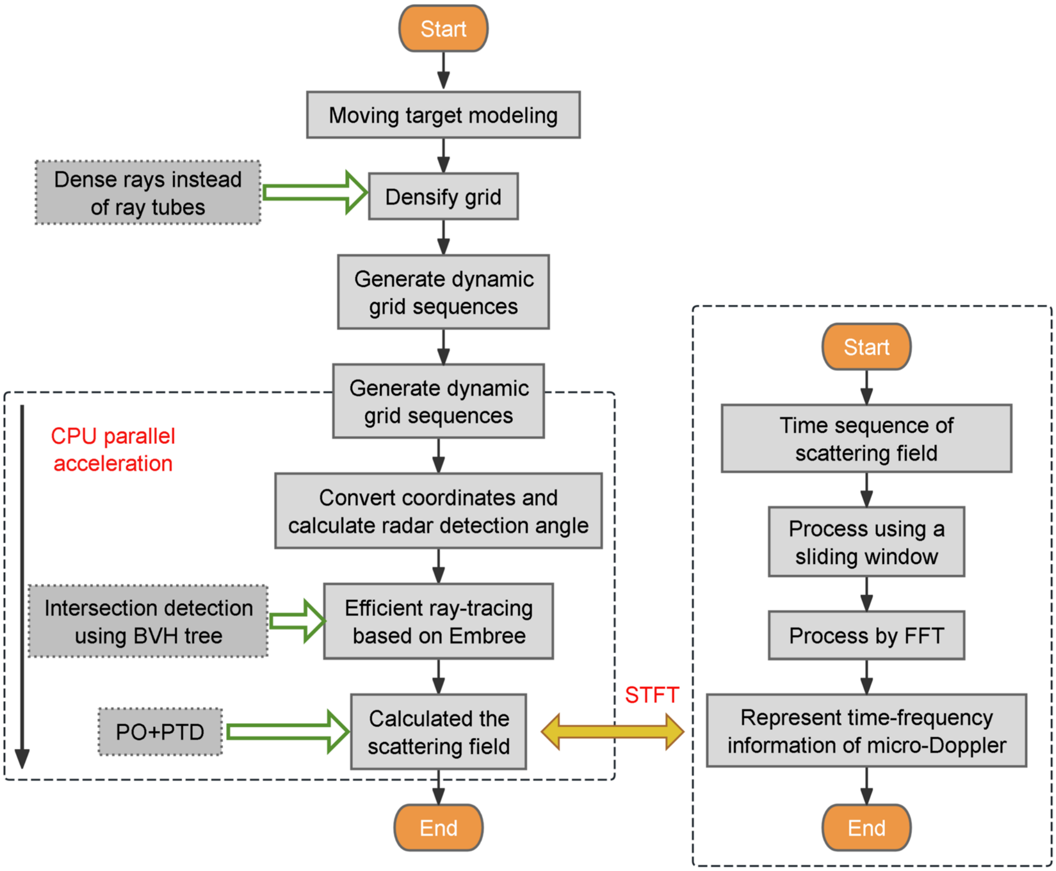

Fig. 4. The flowchart of the efficient SBR method proposed in this paper.

rotation of the cone and the spin of the helicopter rotor. In addition, the strong scattering characteristics in the instantaneous high-resolution range profile (HRRP) were also simultaneously used for comparative analysis. All simulations were conducted on a personal computer with Intel (R) Core (TM) i7-14700KF 3.4 GHz CPU and 64 GB RAM.

Comparison of calculation accuracy and efficiency

Firstly, the trihedral corner reflector was selected as the benchmark object to verify the accuracy of all EM algorithms through measured scattering fields in a microwave anechoic chamber. In Fig. 6a , we conducted RCS testing and simulation comparison on a trihedral corner reflector with a right-angle edge of 200 mm and a thickness of 2 mm (as shown in Fig. 5a) that rotated 35° in the pitch direction. In this validation, all methods showed good agreement with the measurement. Specifically, MLFMM exhibits the best consistency performance. The simulation result of our method is similar to RL-GO, and the difference between the two and measurement is within an acceptable range without significant difference. The simulation result of RaytrAMP maintain good accuracy at most azimuth angles, but exhibit a 3 dB deviation under grazing incidence. Therefore, MLFMM and RL-GO were used to compare the accuracy and efficiency with our method in the following studies.

In addition, RaytrAMP achieves extremely high simulation speed through GPU parallel acceleration (C++ AMP) and linear BVH structure. In order to investigate the computational efficiency comparison between CPU based and GPU based SBR methods, the RCS comparison between the two methods for the scaled-down bomber model (as shown in Fig. 5b) was conducted. In Fig. 6b , the simulation results of two methods have good consistency with the RL-GO based on similar principle. During the simulation process, RaytrAMP consumed 258 seconds and occupied 4 GB of memory, and our method consumed 214 seconds and occupied 42 GB of memory. Overall, our method based CPU parallel has a significant memory consumption, but it has a slight advantage in computational efficiency compared to RaytrAMP based GPU parallel.

In Fig. 6, the motion processes of four typical targets are simulated to evaluate the accuracy and efficiency of our method compared to MLFMM and RL-GO when calculating the dynamic RCS. To measure the degree of deviation between our method and other solutions, we introduced the mean absolute error $\mu = \frac{1}{N}\sum_{i=1}^{N} x_i$ and the standard deviation $\sigma = \sqrt{\frac{1}{N-1}\sum_{i=1}^{N}(x_i - \mu)^2}$. Where, x_i is the absolute value of the RCS difference between our method and other solutions, *N* is the total number of calculations during the motion process. Fig. 6c shows the dynamic RCS comparison of a combined cube (as shown in Fig. 5c) rotating around the *y*-axis at an angular velocity of $\pi/2$ rad/s under HH-polarization, where the incident frequency is 10 GHz and the elevation angle and azimuth angle of radar are $\theta_r = 90^\circ$ and $\varphi_r = 0^\circ$. Fig. 6d shows the dynamic RCS comparison of a trihedral corner reflector with a right-angle side of 1 m (as shown in Fig. 5d), which rotates around $\mathrm{u} = [1, -1, 0]^{\mathrm{T}}$ at an angular velocity of $\pi/9$ rad/s under HH-polarization. Where the incident frequency is 6 GHz and the elevation angle and azimuth angle of radar are $\theta_r = 45^\circ$ and $\varphi_r = 0^\circ$. Fig. 6e shows the dynamic RCS comparison of a missile (as shown in Fig. 5e) under VV-polarization. Where the incident frequency is 10 GHz and the radar

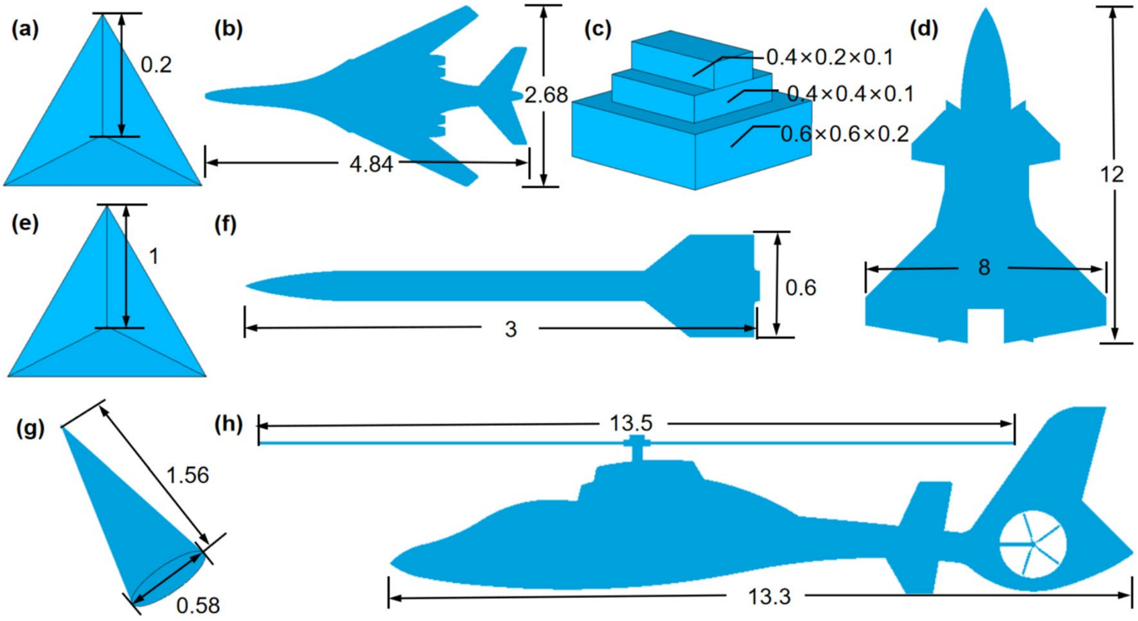

Fig. 5. The geometric models used for simulation: **(a)** 0.2-meter trihedral corner reflector. **(b)** Scale-down bomber model. **(c)** Combined cube. **(d)** 1-meter trihedral corner reflector. **(e)** Missile. **(f)** Aircraft. **(g)** Cone. **(h)** Helicopter. (Unit: m).

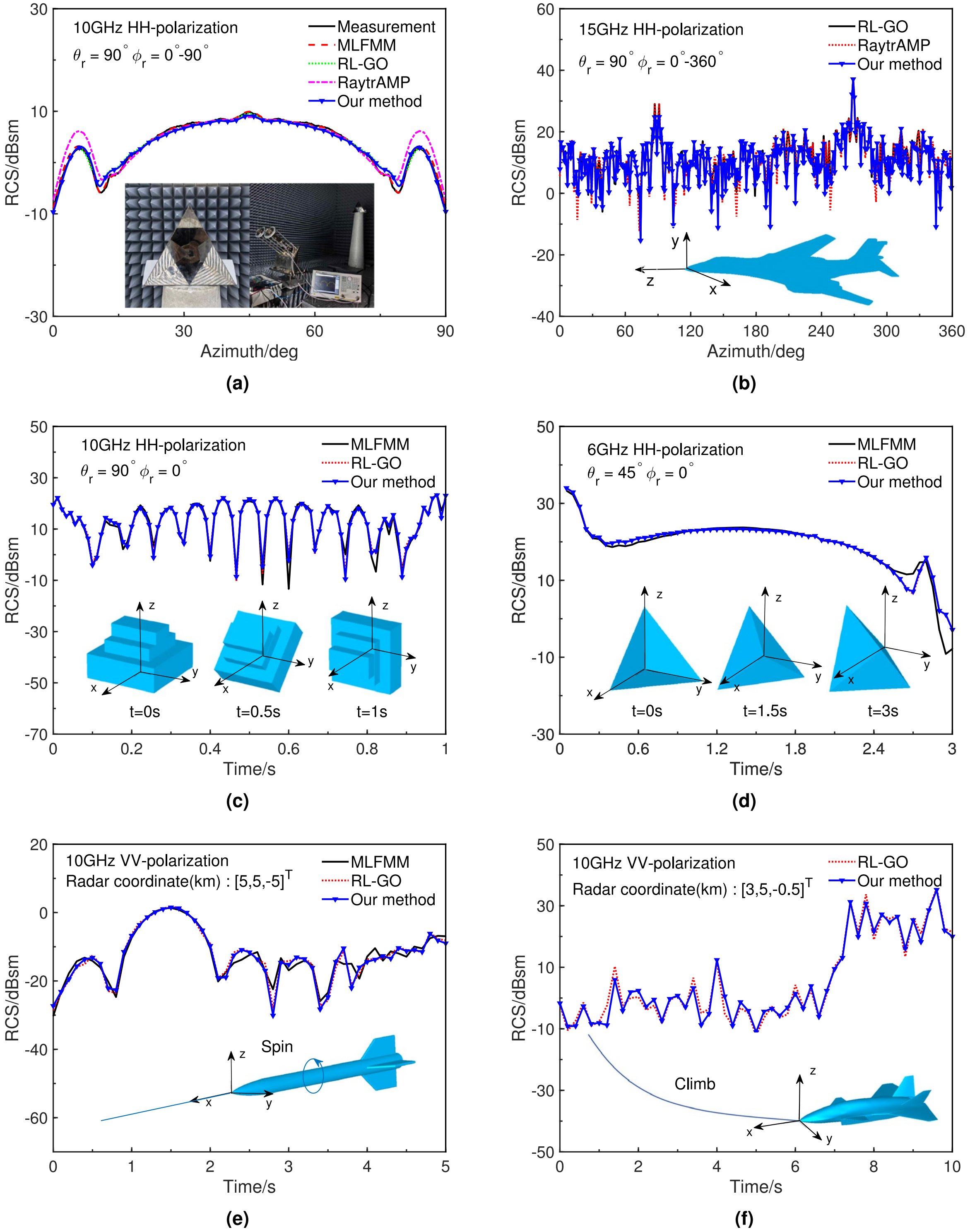

Fig. 6. The target RCS varies with the azimuth angle: **(a)** A 0.2-metre trihedral corner reflector. **(b)** A scale-down bomber model. Dynamic RCS of moving targets: **(c)** A rotating combined cube. **(d)** A rotating trihedral corner reflector. **(e)** A spin-propelled missile. **(f)** A climbing airplane.

coordinate is $[5,5,-5]^{\mathrm{T}}$(km). The missile is propelled forward at a speed of 680 m/s while performing a spin motion of 10π rad/s along the x-axis. Fig. 6f shows the dynamic RCS comparison of an aircraft (as shown in Fig. 5f) during a 10-second climb motion under VV-polarization. Where the incident frequency is 10 GHz and the radar coordinate is $[3,5,-0.5]^{\mathrm{T}}$(km). During this climb process, the variation of the aircraft's pitch angle over time can be expressed as $-0.3(t-10)^2+30$. Meanwhile, the horizontal speed of the aircraft remains at 500 m/s.

	MLFMM and Our Method		RL-GO and Our Method	
	μ	σ	μ	σ
Fig. 6c	1.17	1.89	0.47	0.62
Fig. 6d	1.51	2.88	0.05	0.11
Fig. 6e	1.56	1.54	0.64	0.56
Fig. 6f	/	/	1.52	1.36

Table 1. The statistical error between our method and other solutions.

	Method	MLFMM	RL-GO	Our method	Speedup
Fig. 6c	No. of facets	245,386	556	46,226	6.13
	Runtime	1h40min	49s	8s	
Fig. 6d	No. of facets	30,184	42	312,875	5.47
	Runtime	19min30s	1min44s	19s	
Fig. 6e	No. of facets	39,224	19338	626,660	37.69
	Runtime	8h6min18s	14min27s	23s	
Fig. 6f	No. of facets	/	213,288	1,317,198	18.94
	Runtime	/	22min6s	1min10s	

Table 2. Comparison of computational costs between our method and other solutions.

By referring to the calculation results obtained from MLFMM and RL-GO as benchmark values, the μ and σ obtained by our method are shown in Table 1. The μ and σ of our method compared with the RL-GO whose principle is similar are between 0.05∼1.52 and 0.11∼1.36, respectively. And those compared with the MLFMM which is a more accurate algorithm are between 1.17∼1.56 and 1.54∼2.88, respectively. Obviously, the comparisons of the four examples all indicate that our method has good consistency with the other two different methods, which proves the effectiveness of our proposed method for accurate prediction. The computational costs of four examples using three different methods are shown in Table 2. It can be seen from the results that although our method requires a larger number of facets, the calculation speed has been significantly improved. Compared to RL-GO, the speedup ratio can reach several times or even tens of times. And as the number of facets and time sampling increase, the acceleration effect becomes more pronounced. In summary, it indicates that our method can maintain extremely high computational efficiency while ensuring computational accuracy. In particular, when the high-density temporal sampling are required by the subsequent time-frequency analysis, our method can achieve superior computational efficiency.

Micro-Doppler of moving targets

The physical essence of the micro-Doppler effect lies in that the micro-motion of target causes the radial velocity of the scattering points relative to the radar to change periodically. Therefore, we can understand and analyze micro-motion effects more intuitively by combining the strong scattering points in the instantaneous HRRP with the micro-Doppler information. In Fig. 7, the micro-Doppler spectrum of the cone rotating about a fixed axis and the instantaneous HRRPs at 0.1 s, 0.23 s, and 0.4 s are simulated using our method. The cone along the x-axis rotates around $\mathrm{u} = [0.2, 1, 0]^{\mathrm{T}}$ at an angular velocity of 2π rad/s. The incident direction of the EM wave is shown in the figure, with a center frequency of 10 GHz and a polarization mode of HH. It can be seen from Fig. 7b -7d that the equivalent strong scattering points are concentrated at the vertex (point 1), conical surface (points 2, 3, 5), and base (point 4) of the cone. In Fig. 7a, the white box, black box, and yellow box represent the micro-motion of the vertex, conical surface, and base, respectively.

Figure 8 shows the simulated micro-Doppler spectrum and instantaneous HRRPs of a helicopter under 10 GHz and VV-polarization. The angular velocity of the helicopter rotor is 8π rad/s. In Fig. 8a, the bright lines concentrated around 0 Hz are caused by non-rotating components of the fuselage. These non-rotating components do not move relative to the EM wave in the incident direction, and therefore do not produce frequency shift. The high-speed rotational motion of the rotor causes a micro-Doppler effect with a large bandwidth.

Due to the swept-back configuration of the rotor blade with a sweep angle of 18°, the blade and tip are discussed separately. The leading edge and trailing edge of the blade are parallel. During rotation, the leading edge of forward blade and the trailing edge of backward blade will simultaneously become perpendicular to the incident radar wave. Therefore, both cause the micro-Doppler glint strips at the same time. Specifically, the leading edge causes a positive micro-Doppler glint strip (Point 3), while the trailing edge causes a negative micro-Doppler glint strip (Point 2), with each occurring four times within one complete rotation period (0.25 s). Because the sweep angle of the tip is 18°, the micro-Doppler glint strip (Point 5, Point 7) caused by it lags behind the blade by 0.0125 s. Due to the higher scattering intensity of the leading edge compared to the trailing edge, the spectral brightness of the positive micro-Doppler glint strips is more pronounced than that of the negative

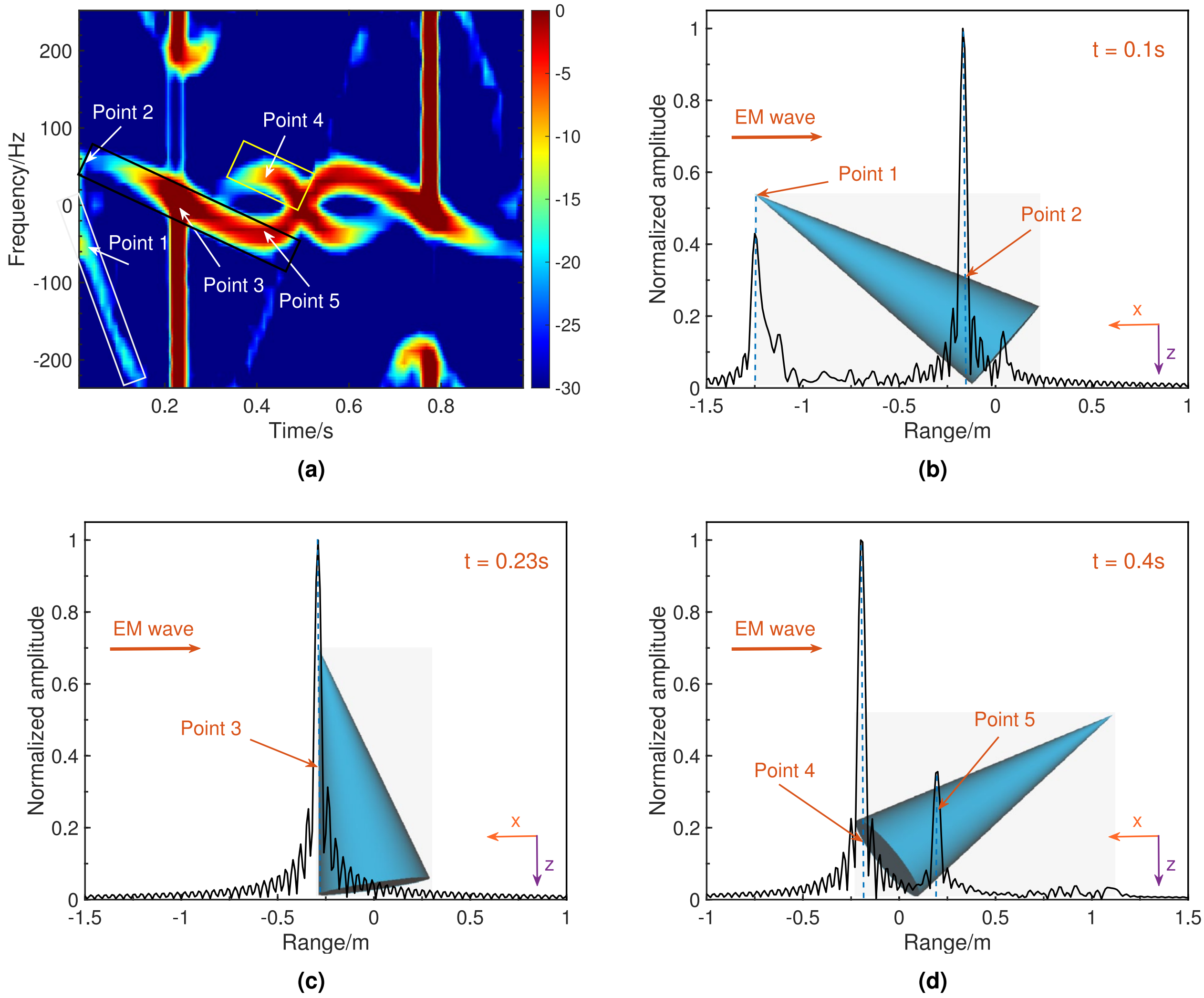

Fig. 7. **(a)** Micro-Doppler spectrum of a rotating cone and **(b-d)** instantaneous HRRPs at 0.1s, 0.23s, and 0.4s.

micro-Doppler glint strips. Obviously, the micro-Doppler spectrum can reflect the parameter characteristics of moving parts and can serve as an important basis for identifying targets.

Conclusion

In conclusion, this work proposes an efficient SBR method in the rapid solution and analysis of dynamic RCS for moving targets. The core idea is to reduce the number of tracked rays by using dense rays instead of ray tubes and to accelerate the intersection detection between rays and targets through the CPU-based ray-tracing kernel Embree. The entire solution process is carried out on the CPU, avoiding the disadvantages of OptiX's high dependence on NVIDIA's GPU hardware and the complexity of CPU-GPU data transmission. Besides, we decomposed the calculation process of the RCS for moving targets into multiple independent subtasks and executed them in parallel to fully leverage the parallel computing capabilities of multi-core CPUs. In our simulation comparison, our method has good consistency with both the measurement and the two methods in FEKO. This demonstrates the effectiveness of our proposed SBR method for accurate prediction. Meanwhile, there has been a significant improvement in computational efficiency slightly better than RaytrAMP based GPU parallel, with a speedup ratio of several times or even dozens of times compared to RL-GO. The proposed SBR method achieves a high level of computational efficiency while ensuring accuracy, thus meeting the requirements for fast and accurate prediction of dynamic RCS of moving targets. Finally, we conduct simulation and analysis on the micro-Doppler characteristics of moving targets by combining the strong scattering point distribution of instantaneous HRRPs. This approach can accurately reflect the frequency modulation and parameter characteristics of moving parts. In the future, we hope to conduct research on the classification and recognition of moving targets based on the method proposed in this paper.

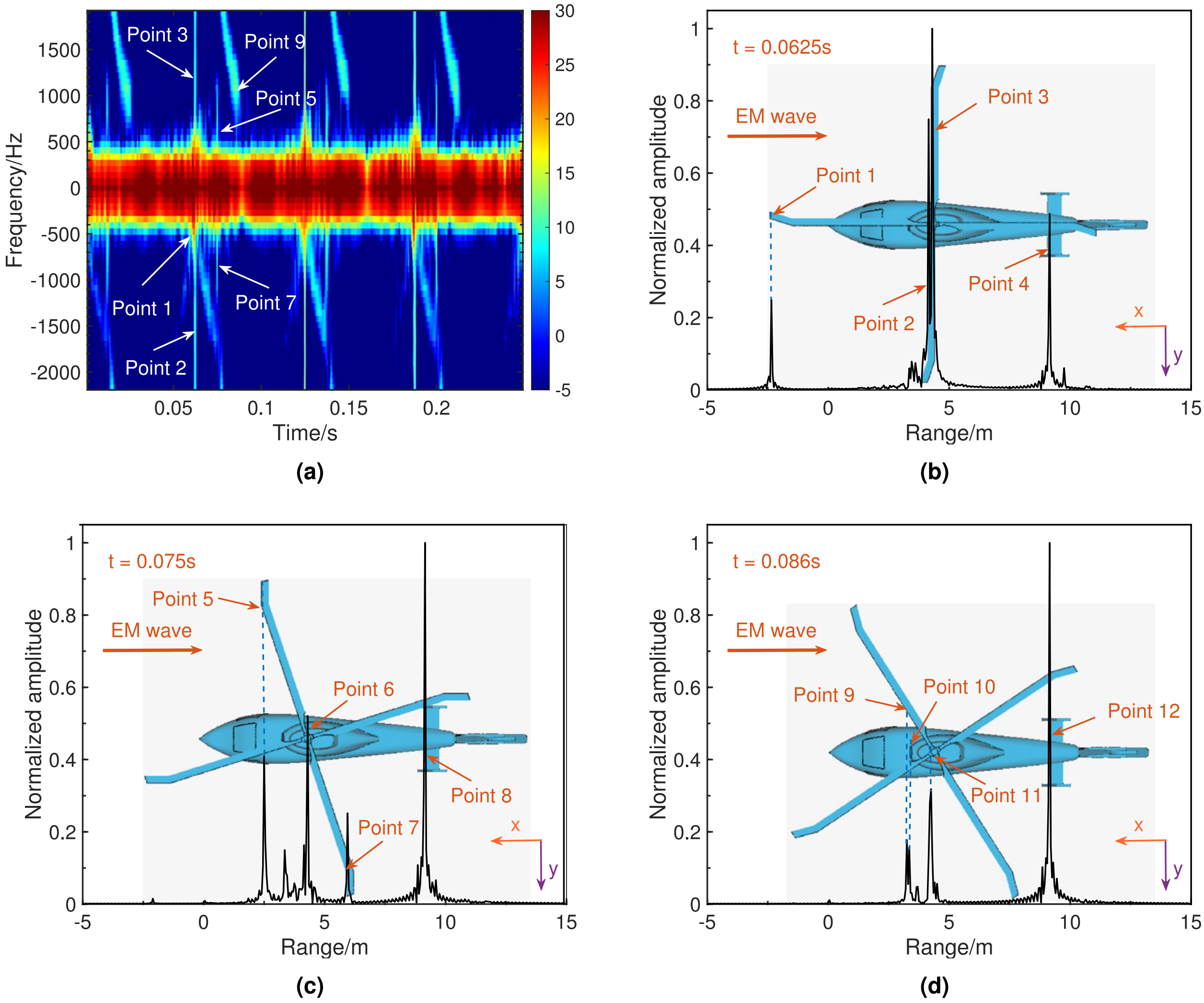

Fig. 8. **(a)** Micro-Doppler spectrum of a hovering helicopter and **(b-d)** instantaneous HRRPs at 0.0625s, 0.075s, and 0.086s.

Data availability

All data generated or analysed during this study are included in this published article.

Received: 29 April 2025; Accepted: 18 December 2025

References

1. Huang, Y., Zhao, Z., Nie, Z. & Liu, Q.-H. Dynamic volume equivalent sbr method for electromagnetic scattering of targets moving on the sea. *IEEE Trans. Antennas Propag.* **71**, 3509–3519 (2023).
2. Zhou, Z. & Huang, J. Z-folding aircraft electromagnetic scattering analysis based on hybrid grid matrix transformation. *Sci. Rep.* **12**, 4452 (2022).
3. Lee, D.-Y., Lee, J.-I. & Seo, D.-W. Dynamic rcs estimation according to drone movement using the mom and far-field approximation. *J. Electromagn. Eng. Sci.* **21**, 322–328 (2021).
4. Delgado, C., Garcia, E., Lozano, L. & Catedra, M. F. Full-wave computation of monostatic rcs using ray-tracing and adaptive macro-basis functions. *IEEE Trans. Antennas Propag.* **69**, 3381–3388 (2021).
5. Kuang, L. & Jin, Y.-Q. Bistatic scattering from a three-dimensional object over a randomly rough surface using the fdtd algorithm. *IEEE Trans. Antennas Propag.* **55**, 2302–2312 (2007).
6. Jo, M., Park, W., Kim, M. & Lee, W. Accelerated finite element method solver for rcs analysis using cuda-based parallel computing. *IEEE Access* **12**, 120375–120388 (2024).
7. Algar, M.-J., Lozano, L., Moreno, J., González, I. & Cátedra, F. An efficient hybrid technique in rcs predictions of complex targets at high frequencies. *J. Comput. Phys.* **345**, 345–357 (2017).
8. Corbel, C., Bourlier, C., Pinel, N. & Chauveau, J. Rough surface rcs measurements and simulations using the physical optics approximation. *IEEE Trans. Antennas Propag.* **61**, 5155–5165 (2013).
9. de Adana, F. et al. Calculation of the rcs from the double reflection between planar facets and curved surfaces. *IEEE Trans. Antennas Propag.* **51**, 2509–2512 (2003).

10. Shah, M. A., Tokgoz, C. & Salau, B. A. Radar cross section prediction using iterative physical optics with physical theory of diffraction. *IEEE Trans. Antennas Propag.* **70**, 4683–4690 (2022).
11. Meana, J. G., Martinez-Lorenzo, J. A., Las-Heras, F. & Rappaport, C. Wave scattering by dielectric and lossy materials using the modified equivalent current approximation (meca). *IEEE Trans. Antennas Propag.* **58**, 3757–3761 (2010).
12. Huo, J., Xu, L., Shi, X. & Yang, Z. An accelerated shooting and bouncing ray method based on gpu and virtual ray tube for fast rcs prediction. *IEEE Antennas Wirel. Propag. Lett.* **20**, 1839–1843 (2021).
13. Cong, Z., He, Z. & Ding, D.-Z. Rcs calculation of electrically large targets by iterative bidirectionally ray tracing method. *IEEE Antennas Wirel. Propag. Lett.* **21**, 2427–2431 (2022).
14. Dong, C., Guo, L., Meng, X. & Li, H. An improved go-po/ptd hybrid method for em scattering from electrically large complex targets. *IEEE Trans. Antennas Propag.* **70**, 12130–12138 (2022).
15. Dong, C., Guo, L. & Meng, X. Application of cuda-accelerated go/po method in calculation of electromagnetic scattering from coated targets. *IEEE Access* **8**, 35420–35428 (2020).
16. Dong, C.-L., Guo, L.-X., Meng, X. & Wang, Y. An accelerated sbr for em scattering from the electrically large complex objects. *IEEE Antennas Wirel. Propag. Lett.* **17**, 2294–2298 (2018).
17. Feng, T.-T. & Guo, L.-X. An improved ray-tracing algorithm for sbr-based em scattering computation of electrically large targets. *IEEE Antennas Wirel. Propag. Lett.* **20**, 818–822 (2021).
18. Liu, H., Wei, B., Wang, H. & Wei, H. Improved bidirectional ray-tracing sbr algorithm based on bvh acceleration. *IEEE Antennas Wirel. Propag. Lett.* **23**, 1839–1843 (2024).
19. Meng, W., Li, J., Guo, L.-X. & Yang, Q.-J. An accelerated sbr method for rcs prediction of electrically large target. *IEEE Antennas Wirel. Propag. Lett.* **21**, 1930–1934 (2022).
20. Zhang, M., Zhao, Y., Li, J.-X. & Wei, P.-B. Reliable approach for composite scattering calculation from ship over a sea surface based on fbam and go-po models. *IEEE Trans. Antennas Propag.* **65**, 775–784 (2017).
21. Guo, K.-Y., Zhang, Z., Mou, Y. & Sheng, X.-Q. A semi-analytical scattering model for efficient radar scattering simulation of the composite scenes. *IEEE Trans. Antennas Propag.* **72**, 6843–6848 (2024).
22. Huang, Y., Zhao, Z., Nie, Z. & Liu, Q.-H. Dynamic volume equivalent sbr method for electromagnetic scattering of targets moving on the sea. *IEEE Trans. Antennas Propag.* **71**, 3509–3519 (2023).
23. Xu, G., Dong, C., Zhao, T., Yin, H. & Chen, X. Acceleration of shooting and bouncing ray method based on optix and normal vectors correction. *PLoS One* **16**, e0253743 (2021).
24. Meng, W. et al. An improved shooting and bouncing ray method based on blend-tree for em scattering of multiple moving targets and echo analysis. *IEEE Trans. Antennas Propag.* **72**, 2723–2737 (2024).
25. Xi, Y., Li, J., Guo, L., Meng, W. & Wen, S. Fast solution of scattering and micro-doppler features from moving target using a tailored shooting and bouncing ray method. *Remote Sens.* **15**, 5724 (2023).
26. Fei, Z., Yang, Y., Jiang, X., Zhao, Q. & Chen, X. Dynamic electromagnetic scattering simulation of tilt-rotor aircraft in multiple modes. *Sensors* **23**, 7606 (2023).
27. Zhou, Z. & Huang, J. Study of rcs characteristics of tilt-rotor aircraft based on dynamic calculation approach. *Chin. J. Aeronaut.* **35**, 426–437 (2022).
28. Guay, R., Drolet, G. & Bray, J. R. Measurement and modelling of the dynamic radar cross-section of an unmanned aerial vehicle. *IET Radar Sonar Navig.* **11**, 1155–1160 (2017).
29. Sen, K., Aksimsek, S. & Kara, A. Dynamic rcs modeling and aspect angle analysis for highly maneuverable uavs. *Aerospace* **11**, 775 (2024).
30. Wald, I., Woop, S., Benthin, C., Johnson, G. S. & Ernst, M. Embree: A kernel framework for efficient cpu ray tracing. *ACM Trans. Graph.* **33**, 1–8 (2014).

Author contributions

W.W. proposed the main idea of this work, W.W. and J.J. developed the algorithm code, K.C. and G.C. conducted the calculations, S.S. and Z.G. analyzed the results. W.W and Y.M. wrote the manuscript based on input from all authors. All authors reviewed the manuscript.

Declarations

Competing interests

The authors declare no competing interests.

Additional information

Correspondence and requests for materials should be addressed to Y.M.

Reprints and permissions information is available at www.nature.com/reprints.

Publisher's note Springer Nature remains neutral with regard to jurisdictional claims in published maps and institutional affiliations.